Understanding the Mössbauer spectrum of magnetite below the Verwey transition: *Ab initio* calculations, simulation, and experiment

R. Řezníček,[1,2,*] V. Chlan,[1] H. Štěpánková,[1] P. Novák,[3] J. Żukrowski,[4] A. Kozłowski,[5] Z. Kąkol,[5] Z. Tarnawski,[5] and J. M. Honig[6]

[1]*Faculty of Mathematics and Physics, Charles University, V Holešovičkách 2, 180 00 Prague 8, Czech Republic*
[2]*Faculty of Physics and Earth Sciences, University of Leipzig, Linnéstrasse 5, D-04103 Leipzig, Germany*
[3]*Institute of Physics of ASCR, Cukrovarnická 10, 162 53 Prague 6, Czech Republic*
[4]*Academic Centre for Materials and Nanotechnology, AGH University of Science and Technology, aleja Mickiewicza 30, 30-059 Kraków, Poland*
[5]*Faculty of Physics and Applied Computer Science, AGH University of Science and Technology, aleja Mickiewicza 30, 30-059 Kraków, Poland*
[6]*Department of Chemistry, Purdue University, 560 Oval Drive, West Lafayette, Indiana 47907-2084, USA*

(Received 29 August 2017; revised manuscript received 10 October 2017; published 13 November 2017)

Magnetite is often the subject of Mössbauer spectroscopy experiments either as a part of fundamental research of this compound or during various geological studies. However, the complicated structure of the low-temperature phase of magnetite exhibits 24 crystallographic iron sites, which presents a considerable obstruction for spectrum interpretation. In this work, we carried out *ab initio* calculations to obtain a complete set of hyperfine parameters of all the sites, and we used these parameters to simulate the corresponding Mössbauer spectrum. Simulation analysis suggested an approximation of the spectrum by four sextets. Parameters of these four sextets were calculated, and the approximation was shown to be appropriate. Further, the Mössbauer spectrum of a high-quality synthetic single crystal of magnetite was measured at 4 K, allowing for a comparison of the theoretical results with the experimental data. Finally, the four-sextet approximation was successfully applied to fit the measured spectrum.

DOI: 10.1103/PhysRevB.96.195124

I. INTRODUCTION

The formal composition of magnetite can be written as $[Fe^{3+}]_A[Fe^{2+}Fe^{3+}]_B O_4^{2-}$, where A denotes iron sites surrounded by oxygen ions forming tetrahedra and B corresponds to the iron ions inside octahedra formed by the nearest oxygen ions. Apparently, the B sublattice exhibits mixed-valence character. Magnetite has been drawing the attention of physicists since 1939 when the Verwey phase transition was found [1]. This transition occurring at temperature $T_V \approx 120$ K is accompanied by a step change in electrical conductivity. When temperature drops below T_V, the inverse cubic ($Fd\bar{3}m$) spinel structure of magnetite reduces its symmetry and transforms into the monoclinic Cc structure. Accordingly, the cubic crystal splits into 12 magnetically nonequivalent monoclinic domains [2]. In the high-temperature cubic phase, all A sites are crystallographically equivalent, and the same holds for all B sites. On the other hand, there are 8 different groups of crystallographically equivalent A sites and 16 different groups of crystallographically equivalent B sites in the low-temperature monoclinic structure. Thus, one of the most interesting open questions concerns the charge ordering of the low-temperature phase [3–6], which has been probed by various means, including the hyperfine methods comprising the Mössbauer spectroscopy [7–11] as well as nuclear magnetic resonance (NMR) [2,12–14].

Recent progress comprises mainly the determination of the crystal-structure parameters of the Cc phase by Senn *et al.* [15]. Based on their data, Senn *et al.* suggested a trimeron model to describe the charge order of the B sublattice. The trimeron consists of three nearest-neighbor Fe(B) ions in a line; the Fe^{2+}-like ion in the trimeron's center donates a part of its minority-spin t_{2g} electron to the two Fe^{3+}-like ions at the trimeron's ends. The trimerons form a complex network, but there are also two groups of crystallographically equivalent Fe(B) sites which do not participate in any trimeron. The publication of Senn *et al.* was followed by several works which employed the structure data for *ab initio* calculations (see Refs. [2,16,17]). The work of Patterson [17] presented an alternative model consisting of Fe(B) ions incorporated either in a broken branched zigzag chain or in pairs with one-electron bonds. On the other hand, Ref. [2] supported the trimeron model as a more adequate description of the electronic structure and grouped the B sites in an 8:5:3 ratio. The first group contains Fe^{3+}-like ions, while the other groups are occupied by Fe^{2+}-like ions.

Despite a significant number of publications concerning the Mössbauer spectroscopy of the low-temperature Cc phase of magnetite, a reliable detailed interpretation of the structure of the spectra is still unavailable because of a significant overlap of the spectral components (sextets) originating from the 24 different groups of iron sites. In this situation, the authors of existing experimental studies of magnetite [7–11,18–21] usually have had to resort to various phenomenological assumptions to be able to decompose their spectra into several sextets. However, the choice of suitable assumptions is difficult from both fundamental and practical points of view since subsequent analysis of the results is bound within the limits determined by the assumptions and a comparison of different studies is complicated if different decomposition approaches are used. Thus, the aim of the present work is to understand the Mössbauer spectra in the context of current knowledge. The *ab initio* calculations based on the density functional theory (DFT) are employed as a primary source of hyperfine

*reznicek@mbox.troja.mff.cuni.cz

parameters for spectrum simulation. The calculation outputs are supplemented with the hyperfine data extracted from ^{57}Fe NMR experiments [2,12,13]. Finally, the analysis of the simulation results allows for an appropriate fit of the experimental Mössbauer spectrum.

II. CALCULATIONS

In order to obtain the hyperfine parameters necessary for the simulation of the Mössbauer spectrum, the WIEN2K software [22] was utilized for the DFT calculations of the electronic structure of the Cc phase of magnetite. We used 9500 ($RK_{\max} = 6.0$) basis functions and 9 k points in the irreducible part of the Brillouin zone. The density of charge was Fourier expanded to $G_{\max} = 16$ Ry$^{\frac{1}{2}}$. The generalized gradient approximation plus U method with $U_{\text{eff}} = 4.5$ eV, $R_{\text{MT}}(\text{Fe}) = 2$ a.u., and $R_{\text{MT}}(\text{O}) = 1.5$ a.u. was employed. The spin-orbit coupling was included in the calculations.

The calculations used the crystal-structure parameters of the Cc phase of magnetite published by Senn *et al.* [15]. Structure optimization was not performed in order to avoid the risk of reaching an incorrect total energy minimum. Thus, consistency with the calculations in Ref. [2] was kept. The average force acting on the ions in the experimental structure was 9.8 mRy a.u.$^{-1}$, while the maximum force was 19.3 mRy a.u.$^{-1}$.

A. Charge density at iron nuclei and isomer shift

The electron charge density at the iron nuclei manifests itself in the Mössbauer spectra as an isomer shift relative to the reference (metallic bcc α-Fe). The charge densities at the iron nuclei at 8 nonequivalent A sites and 16 nonequivalent B sites were determined from the DFT calculations as the density at the radial grid point R_0 closest to the nucleus position (this density is assumed to be constant over the corresponding sphere with radius R_0). The value of $R_0 = 5 \times 10^{-5} a_0$ ($a_0 \approx 5.292 \times 10^{-11}$ m is the Bohr radius) was comparable to the nuclear radius. The resulting charge densities ρ_0 at iron nuclei (and corresponding isomer shifts) are provided in Table I.

Isomer shift δ (expressed in γ source-velocity units) is related to the charge density ρ_0 at the nucleus [23]:

$$\delta = \frac{c}{E_0}\frac{1}{10\epsilon_0} Ze[(R^\star)^2 - R^2](\rho_0 - \rho_{0,\text{Fe}}), \qquad (1)$$

where $\rho_{0,\text{Fe}}$ is the electron charge density at the nuclei in α-Fe, ϵ_0 denotes vacuum permittivity, E_0 represents the energy of the first excited state of the ^{57}Fe nucleus, c is the speed of light, Z stands for the proton number, and R and $R^\star$ are nuclear charge radii of the ^{57}Fe nucleus in the ground state and the first excited state, respectively. Unfortunately, this relation does not allow us to directly obtain the isomer shift from calculated charge densities due to the significant uncertainty of the ^{57}Fe nuclear charge radius $R^\star$ in the excited state [24]. Instead, the following expression has to be used:

$$\delta = \alpha(\rho_0 - \rho_{0,\text{Fe}}), \qquad (2)$$

where the coefficient α is determined by a calibration procedure described, e.g., in Ref. [25]. Our calibration required a calculation of charge densities at iron nuclei in various compounds (including iron oxides) in the same way as for the data in Table I. These values of charge density were then paired with published experimental isomer shifts (see Table II) and utilized for fitting the dependence (2) (see Fig. 1). The fit determined the coefficient value of $\alpha = -0.284 \pm 0.011$ mm s^{-1} e^{-1} a_0^3 ($a_0 \approx 5.292 \times 10^{-11}$ m is the Bohr radius), which is in agreement with the values obtained in Ref. [25] ($\alpha = -0.291 \pm 0.014$ mm s^{-1} e^{-1} a_0^3 for halides and TiFe using the full-potential linearized augmented plane-wave and augmented plane-wave plus local-orbital methods implemented in the WIEN2K software) and Ref. [26] ($\alpha = -0.278 \pm 0.028$ mm s^{-1} e^{-1} a_0^3 for iron complexes using quasirelativistic DFT within the zero-order regular approximation). It should be noted that despite the good agreement with the published coefficient values, it was necessary to perform the calibration with our particular DFT calculation method (including specific parameter settings) rather than just using some of published values because the resulting α value is influenced by the applied DFT calculation method [32,33].

The values of isomer shift obtained from Eq. (2) for particular iron sites in magnetite are included in Table I. The values exhibit a sensitivity to the configuration of $3d$ electrons [30]: $\delta = 0.34$–0.35 mm s^{-1} for Fe^{3+} ions at the A sites, while at the B sites $\delta = 0.48$–0.68 mm s^{-1} for Fe^{3+}-like ions and $\delta = 0.80$–0.97 mm s^{-1} for Fe^{2+}-like ions.

TABLE I. Electron charge density ρ_0 at iron nuclei in magnetite obtained from the DFT calculations together with isomer shift δ derived using Eq. (2) [the ±4% error of the isomer shift is determined by the calibration error of α (see text); $a_0 \approx 5.292 \times 10^{-11}$ m denotes the Bohr radius]. The site numbering is the same as in Ref. [2] and corresponds to site listing order in Ref. [15].

DFT site	Nominal valence state [15]	ρ_0 ($e\,a_0^{-3}$)	$\rho_0 - \rho_{0,\text{Fe}}$ ($e\,a_0^{-3}$)	δ (mm s^{-1})
A1	3+	15308.964	−1.233	0.350
A2	3+	15308.964	−1.233	0.350
A3	3+	15308.951	−1.245	0.354
A4	3+	15308.982	−1.215	0.345
A5	3+	15308.975	−1.222	0.347
A6	3+	15308.991	−1.206	0.342
A7	3+	15308.994	−1.202	0.341
A8	3+	15308.985	−1.211	0.344
B1	2+	15306.875	−3.322	0.943
B2	2+	15306.844	−3.352	0.952
B3	2+	15306.924	−3.273	0.929
B4	2+	15307.382	−2.815	0.799
B5	3+	15308.316	−1.880	0.534
B6	3+	15308.095	−2.101	0.597
B7	2+	15306.885	−3.311	0.940
B8	3+	15308.513	−1.684	0.478
B9	3+	15307.812	−2.385	0.677
B10	3+	15308.095	−2.101	0.597
B11	3+	15308.063	−2.133	0.606
B12	3+	15308.347	−1.849	0.525
B13	2+	15306.805	−3.392	0.963
B14	2+	15307.029	−3.167	0.899
B15	3+	15308.499	−1.697	0.482
B16	2+	15306.790	−3.406	0.967

TABLE II. Calculated electron charge density ρ_0 at iron nuclei accompanied by experimental isomer shift δ_{exp} for various compounds of iron ($a_0 \approx 5.292 \times 10^{-11}$ m denotes the Bohr radius).

Compound	$\rho_0\ (e\,a_0^{-3})$	$\rho_0 - \rho_{0,\mathrm{Fe}}\ (e\,a_0^{-3})$	δ_{exp} (mm s^{-1})
TiFe	15310.829	0.632	-0.145 ± 0.007 [27]
α-Fe	15310.196	0	0
FeAl	15309.133	−1.064	0.272 ± 0.015 [28]
Fe_2O_3	15308.139	−2.058	0.47 ± 0.03 [29]
FeF_3	15307.628	−2.568	0.489 [23]
YIG (a)	15308.219	−1.978	0.57 ± 0.05 [30]
YIG (d)	15308.996	−1.200	0.26 ± 0.05 [30]
$Fe_3O_4(A)$	15308.866	−1.330	0.36 [7]
(above T_V)			0.34 [8]
			0.27 ± 0.03 [9]
$Fe_3O_4(B)$	15307.608	−2.589	0.78 [7]
(above T_V)			0.66 [8]
			0.67 ± 0.03 [9]
FeS	15307.176	−3.020	1.1 ± 0.1 [30]
FeF_2	15305.414	−4.783	1.467 [31]
			1.40 ± 0.05 [30]

B. Electric field gradient at iron nuclei

Another characteristic of the electronic structure influencing the Mössbauer spectra is the electric field gradient (EFG) tensors at particular iron sites. The EFG tensors obtained from the DFT calculations are provided in Table III, expressed in the orthorhombic coordinate system [34] (as tensor elements $V_{\alpha\alpha'}; \alpha,\alpha' = a,b,c$) as well as in a canonical form (as diagonal elements V_{zz}, V_{yy}, and V_{xx}), together with the asymmetry parameters [$\eta = (V_{xx} - V_{yy})/V_{zz}$] and principal axes ($\vec{v}_{zz}$, $\vec{v}_{yy}$, and $\vec{v}_{xx}$) of the tensors. Visualization of the EFG tensors is shown in Fig. 2 for the B sites and in Fig. 1 of the Supplemental Material [35] for the A sites: the tensors are represented by objects drawn in the elementary cell; the following formula determines the distance r of the object surface from a particular iron-ion site:

$$r = C[V_{aa}\vartheta_a^2 + V_{bb}\vartheta_b^2 + V_{cc}\vartheta_c^2 + 2(V_{ab}\vartheta_a\vartheta_b + V_{ac}\vartheta_a\vartheta_c + V_{bc}\vartheta_b\vartheta_c)], \quad (3)$$

where ϑ_α, $\alpha = a,b,c$, stands for direction cosines with respect to the orthorhombic axes and C is a scaling coefficient (common for all sites in the plot). The figures illustrate the size of the EFG at particular sites, as well as the orientation of the principal axes of the tensors. The EFG at the Fe^{3+}(A) ions is small because of the nearly spherical symmetry of their electronic configuration. The complex situation concerning the B sites, which is depicted in Fig. 2, can be understood in the context of trimerons. Obviously, the EFG at the trimeron central ions is much larger than at the end ions, and the principal axis related to the smallest eigenvalue of the corresponding EFG tensor of the central ion is roughly collinear with the axis of the trimeron. This conforms well with the assumptions based on the electronic structure of trimerons: the minority-spin charge density encompassing the central Fe^{2+}-like ions is significantly anisotropic as the charge is located in the t_{2g} orbital corresponding to the trimeron axis. Concerning the Fe^{3+}-like end ions, the approximately spherical symmetry of the electron density is impacted only by the partial charge donated by the central ions. (When the

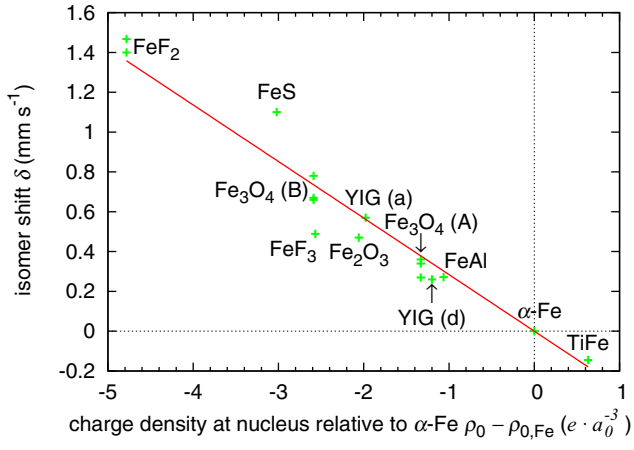

FIG. 1. Isomer shift calibration. The values from Table II are represented by the points; the line corresponds to a fit of expression (2). The a and d crystallographic sites of yttrium iron garnet (YIG) are distinguished. The labels Fe_3O_4 (A) and Fe_3O_4 (B) refer to the A and B sites of the high-temperature phase of magnetite, respectively. ($a_0 \approx 5.292 \times 10^{-11}$ m is the Bohr radius.)

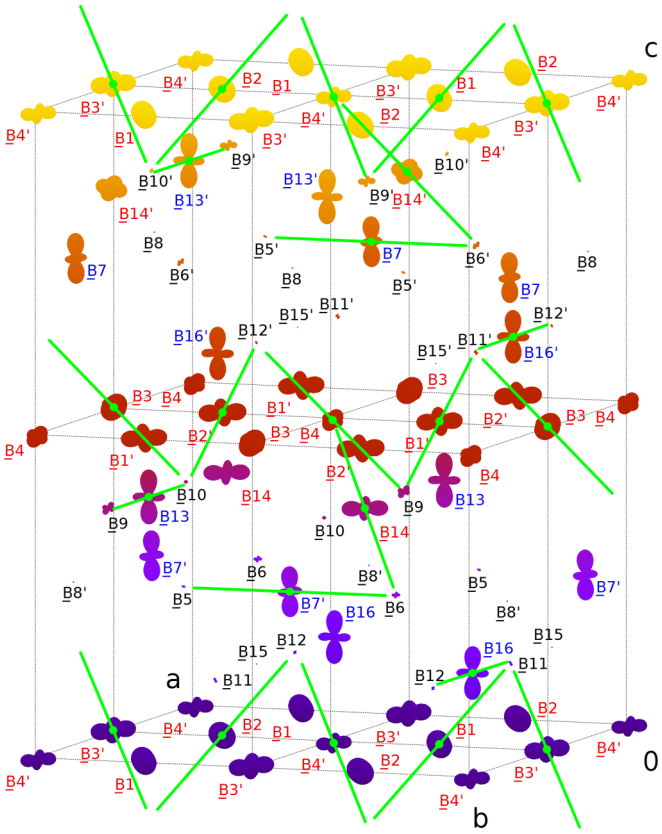

FIG. 2. Visualization of the EFG tensors at Fe(B) sites in the elementary cell (scaling coefficient $C = 0.05$ Å $\times 10^{-21}$ V^{-1} m^2). Trimerons [15] are highlighted by the green lines. The site numbering is the same as in Ref. [2] and corresponds to site listing order in Ref. [15]; primes denote the sites generated by the ac-glide symmetry. (Surface color corresponding to the z coordinate is to improve clarity.)

TABLE III. The EFG tensors at iron sites in Cc phase of magnetite determined by the DFT calculations. See the text for symbol definitions. The site numbering is the same as in Ref. [2] and corresponds to site listing order in Ref. [15].

Site	$V_{aa}(\times 10^{21}\,\mathrm{V\,m^{-2}})$	$V_{bb}(\times 10^{21}\,\mathrm{V\,m^{-2}})$	$V_{cc}(\times 10^{21}\,\mathrm{V\,m^{-2}})$	$V_{ab}(\times 10^{21}\,\mathrm{V\,m^{-2}})$	$V_{ac}(\times 10^{21}\,\mathrm{V\,m^{-2}})$	$V_{bc}(\times 10^{21}\,\mathrm{V\,m^{-2}})$	$V_{zz}(\times 10^{21}\,\mathrm{V\,m^{-2}})$	$V_{yy}(\times 10^{21}\,\mathrm{V\,m^{-2}})$	$V_{xx}(\times 10^{21}\,\mathrm{V\,m^{-2}})$	η	Principal axis $\vec{v}_{zz}$	Principal axis $\vec{v}_{yy}$	Principal axis $\vec{v}_{xx}$
A1	1.522	−1.294	−0.228	−0.298	−0.395	−0.439	1.621	−1.509	−0.112	0.862	(0.979, −0.071, −0.192)	(-0.137, −0.923, −0.359)	(0.152, −0.378, 0.913)
A2	0.739	−0.573	−0.166	0.404	0.211	−0.752	−1.250	0.853	0.397	0.365	(-0.221, 0.781, 0.585)	(0.962, 0.274, −0.004)	(0.163, −0.561, 0.811)
A3	0.286	0.344	−0.630	−0.367	0.256	0.508	−0.965	0.724	0.242	0.499	(0.298, 0.417, −0.859)	(0.561, −0.804, −0.196)	(-0.772, −0.423, −0.473)
A4	0.289	0.166	−0.455	−0.235	0.603	1.415	−1.778	1.344	0.433	0.512	(0.287, 0.586, −0.758)	(0.205, 0.735, 0.646)	(0.936, −0.341, 0.091)
A5	−0.839	0.568	0.272	−0.096	1.038	0.662	−1.550	1.298	0.252	0.675	(0.816, 0.206, −0.540)	(0.323, 0.612, 0.722)	(0.479, −0.764, 0.433)
A6	−0.472	−0.127	0.599	−0.259	−0.363	−0.711	1.055	−0.937	−0.118	0.776	(-0.122, −0.492, 0.862)	(0.673, 0.598, 0.436)	(0.729, −0.633, −0.258)
A7	−1.434	1.572	−0.138	−0.426	0.050	0.651	1.838	−1.509	−0.329	0.642	(0.118, −0.944, −0.308)	(0.981, 0.159, −0.111)	(0.154, −0.289, 0.945)
A8	−1.162	1.104	0.059	−0.035	0.237	−0.035	−1.207	1.106	0.101	0.832	(0.983, 0.012, −0.184)	(-0.019, 0.999, −0.038)	(0.183, 0.041, 0.982)
B1	0.223	6.949	−7.171	−9.551	−0.314	−0.832	13.723	−7.666	−6.058	0.117	(-0.577, 0.816, −0.024)	(0.436, 0.332, 0.836)	(0.691, 0.472, −0.548)
B2	0.622	6.221	−6.843	−10.170	−0.330	−0.857	13.980	−7.784	−6.196	0.114	(-0.605, 0.796, −0.023)	(-0.600, −0.475, −0.643)	(0.523, 0.375, −0.765)
B3	−0.485	7.224	−6.738	−9.466	0.389	0.849	13.601	−7.598	−6.003	0.117	(-0.557, 0.830, 0.024)	(0.596, 0.420, −0.684)	(0.578, 0.367, 0.729)
B4	0.841	4.201	−5.042	−7.589	0.845	0.953	10.297	−6.408	−3.889	0.245	(-0.625, 0.780, 0.014)	(0.568, 0.467, −0.677)	(0.535, 0.415, 0.735)
B5	0.897	−1.249	0.352	0.036	0.277	0.133	−1.260	1.016	0.243	0.614	(0.006, −0.997, 0.081)	(0.919, 0.038, 0.391)	(0.393, −0.072, −0.917)
B6	1.079	−0.092	−0.987	1.629	0.700	−1.053	−2.383	2.224	0.158	0.867	(0.422, −0.609, −0.671)	(-0.815, −0.579, 0.012)	(0.396, −0.542, 0.741)
B7	−4.473	−8.621	13.095	0.393	0.297	0.061	13.100	−8.658	−4.441	0.322	(0.017, 0.003, 1.000)	(0.093, −0.996, 0.002)	(0.995, 0.093, −0.017)
B8	−0.123	0.501	−0.379	0.279	−0.023	−0.191	0.642	−0.424	−0.219	0.319	(0.342, 0.922, −0.180)	(-0.155, 0.244, 0.957)	(0.927, −0.300, 0.226)
B9	1.936	0.174	−2.110	−3.495	0.892	1.376	4.662	−3.979	−0.683	0.707	(0.786, −0.618, −0.022)	(0.454, 0.600, −0.659)	(0.421, 0.507, 0.752)
B10	−1.012	0.640	0.372	−0.313	0.039	0.953	1.486	−1.113	−0.373	0.497	(-0.085, 0.759, 0.646)	(0.939, 0.278, −0.203)	(0.334, −0.589, 0.736)
B11	0.023	0.746	−0.769	−0.764	−0.130	−1.024	1.533	−1.445	−0.088	0.885	(0.398, −0.847, 0.354)	(-0.327, −0.491, −0.807)	(0.857, 0.205, −0.472)
B12	−0.571	0.839	−0.268	0.100	−0.312	−0.889	1.363	−0.918	−0.444	0.348	(0.124, 0.861, −0.493)	(0.571, 0.344, 0.745)	(0.812, −0.374, −0.449)
B13	−8.337	−5.836	14.173	−0.328	0.034	0.401	14.181	−8.380	−5.801	0.182	(0.001, 0.020, 1.000)	(0.992, 0.129, −0.004)	(0.129, −0.991, 0.020)
B14	5.018	1.274	−6.291	9.161	0.845	−0.507	12.502	−7.179	−5.323	0.148	(0.775, 0.632, 0.018)	(0.445, −0.526, −0.725)	(-0.448, 0.570, −0.689)
B15	0.160	−0.283	0.124	−0.179	−0.192	−0.139	−0.421	0.338	0.083	0.606	(-0.381, −0.855, −0.353)	(-0.766, 0.078, 0.638)	(0.518, −0.513, 0.685)
B16	−8.531	−5.295	13.826	−0.040	0.025	−0.397	13.835	−8.531	−5.303	0.233	(0.001, −0.021, 1.000)	(1.000, 0.012, −0.001)	(0.012, −1.000, −0.021)

end ion is a part of multiple trimerons, the donated charges from different central ions enter different orbitals; thus, the symmetry of the end ion is affected still only to a small extent.) In the case of Fe^{3+}-like ions B8 and B15, which do not participate in any trimeron, the EFG is the smallest among the B sites as no transferred charge perturbs the symmetry of their electronic configuration.

On the other hand, the results do not support the model of Patterson [17], as can be seen from the Fe(B) pairs not included in the zigzag chain (e.g., B5′–B7): one would expect a relatively similar charge configuration of these ions due to the one-electron bond, but the difference in the EFG at these sites is striking.

C. Hyperfine magnetic fields

The parameters of the hyperfine magnetic field obtained from the DFT calculations and from the ^{57}Fe NMR data [14] were published in our previous work [2] in the form of isotropic parts and anisotropy tensors of the hyperfine field. The present work has to rely on the parameters from the DFT results since they are assigned to particular iron sites with known coordinates in the elementary cell, unlike the data from the NMR experiment, where an attempt at such an assignment was successful only to a limited extent. However, the DFT calculations tend to systematically overestimate isotropic parts $B_{\rm iso}$ as well as the anisotropy characterized by the following parameter:

$$B_{\rm ani} = \sqrt{B_a'^2 + B_b'^2 + B_c'^2}, \tag{4}$$

where B_a', B_b', and B_c' denote elements of the hyperfine field anisotropy tensor in a canonical form. This effect can be compensated for by a renormalization of these parameters in order to match their average with the average of parameters extracted from the experimental data ($i = 1,\ldots,8$ for the A sites, while $i = 1,\ldots,16$ for the B sites):

$$c_{\rm iso} = \frac{\sum_i B_{\rm iso}^{\rm exp}(i)}{\sum_i B_{\rm iso}^{\rm calc}(i)},$$
$$c_{\rm ani} = \frac{\sum_i B_{\rm ani}^{\rm exp}(i)}{\sum_i B_{\rm ani}^{\rm calc}(i)}.$$

The following values of the renormalization coefficients were found: $c_{\rm iso} = 0.96$ and $c_{\rm ani} = 0.32$ [36] in the case of the A sites; $c_{\rm iso} = 0.94$ and $c_{\rm ani} = 0.65$ for the B sites. Now, the hyperfine field $B_{\rm hf}$ for a particular magnetization direction (denoted by direction cosines ϑ_α, $\alpha = a,b,c$, with respect to the orthorhombic coordinates) can be calculated:

$$B_{\rm hf} = c_{\rm iso}B_{\rm iso} + c_{\rm ani}[B_{aa}\vartheta_a^2 + B_{bb}\vartheta_b^2 + B_{cc}\vartheta_c^2 + 2(B_{ab}\vartheta_a\vartheta_b + B_{ac}\vartheta_a\vartheta_c + B_{bc}\vartheta_b\vartheta_c)], \tag{5}$$

where $B_{\alpha\alpha'}$ ($\alpha,\alpha' = a,b,c$) are elements of the hyperfine field anisotropy tensor expressed in the orthorhombic coordinates.

D. Correlations of hyperfine parameters

Hyperfine properties of particular iron ions are closely related to their electronic configuration; thus, their comparison may illustrate how these parameters are mutually correlated in the context of the valence character of the iron ions (quantified in Ref. [2] using the atoms in molecules (AIM) method [37]). While the situation is fairly simple for the A sites, the case of B-site ions is much more interesting (see Fig. 3). The right part of Fig. 3 shows Fe^{3+}-like ions exhibiting a higher isotropic part $B_{\rm iso}$, smaller anisotropy $B_{\rm ani}$, lower EFG [represented by the parameter $V_{\rm ani} = \sqrt{V_{zz}^2 + V_{yy}^2 + V_{xx}^2}$, where $V_{\beta\beta}, \beta = z,y,x$, are EFG tensor eigenvalues, in analogy to Eq. (4)], and smaller isomer shift than the Fe^{2+}-like ions in the left part. This is caused by low minority-spin $3d$ populations of Fe^{3+}-like ions leading to higher spin moment and, consequently, to higher $B_{\rm iso}$. At the same time, orbital moments of these ions are small, resulting into a low hyperfine field anisotropy. The relatively high symmetry of the $3d$ electron distribution of Fe^{3+}-like ions is responsible for the low EFG. An opposite description can be used for the Fe^{2+}-like ions. The overall valence character of the iron ions is reflected by the isomer shift. Clearly, all parameters plotted in Fig. 3 exhibit roughly linear dependence on the valence state of a particular iron ion.

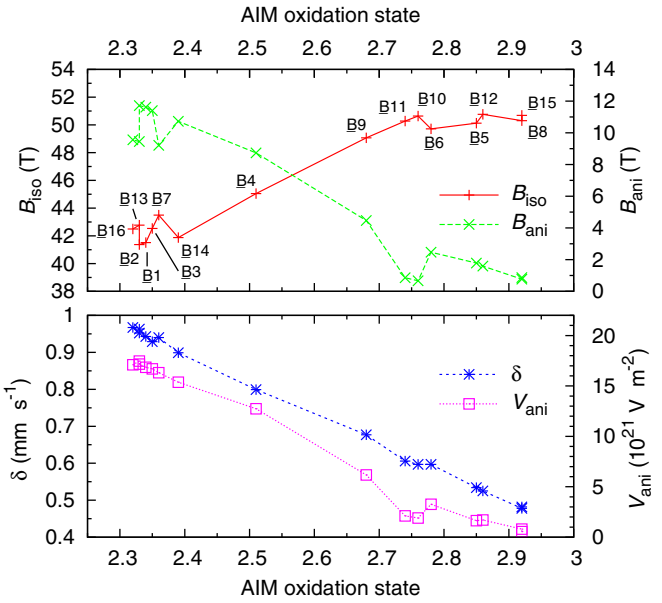

FIG. 3. Renormalized isotropic and anisotropic parts of the hyperfine magnetic field $V_{\rm ani} = \sqrt{V_{zz}^2 + V_{yy}^2 + V_{xx}^2}$ parameter of EFG and isomer shift δ of the B-site iron ions plotted as a function of oxidation state determined by the AIM method in Ref. [2]. The site numbering is the same as in Ref. [2] and corresponds to site listing order in Ref. [15]. The lines serve only to guide the eye.

III. SIMULATION

The hyperfine parameters obtained in Sec. II allowed for a simulation of a zero-field ^{57}Fe Mössbauer spectrum of the Cc phase of magnetite using the FITSUITE 1.1.0.RC.11 software [38]. A single crystal consisting of a single domain (with the magnetization along the easy c axis) in an orientation with the [201] direction parallel to the γ beam was considered. This special orientation results in sextet line-intensity ratio of 3:2:1:1:2:3 [39]. The line broadening was set equal to the natural linewidth $\Gamma_{\rm N}$ for the A sites and to twice the natural linewidth in the case of the B sites, where more significant

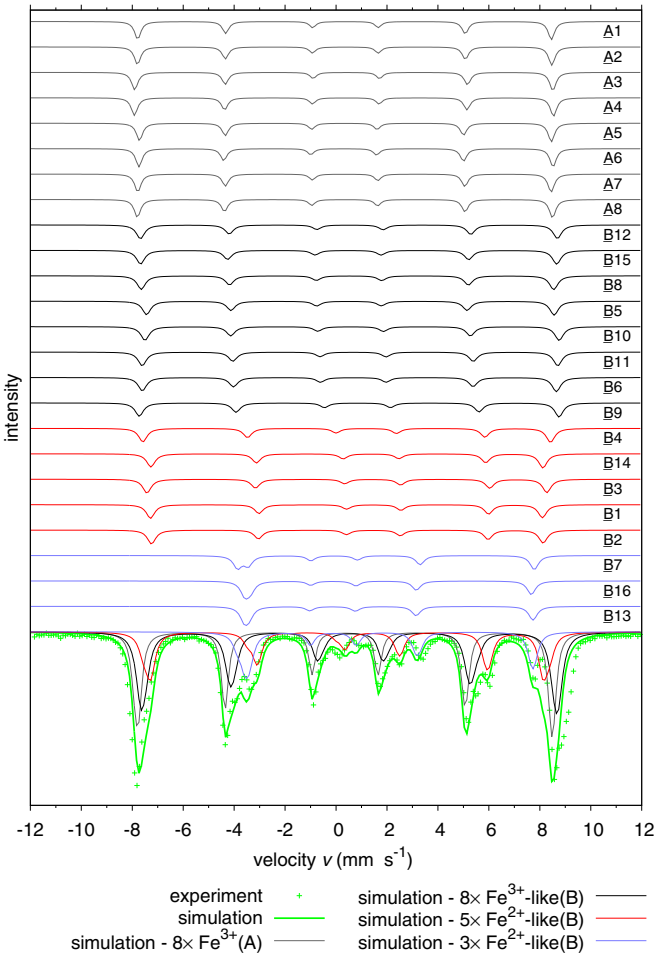

FIG. 4. Simulation of a zero-field ^{57}Fe Mössbauer spectrum (referenced to α-Fe) of a single-domain single-crystal sample of magnetite (in the low-temperature phase) oriented in the [201] direction along the incident γ ray. The site numbering is the same as in Ref. [2] and corresponds to site listing order in Ref. [15]. Black, red, and blue indicate the three groups of Fe(B) subspectra corresponding to the three groups of Fe(B) ions identified in Ref. [2]. The experimental data (see Sec. IV) are given for comparison.

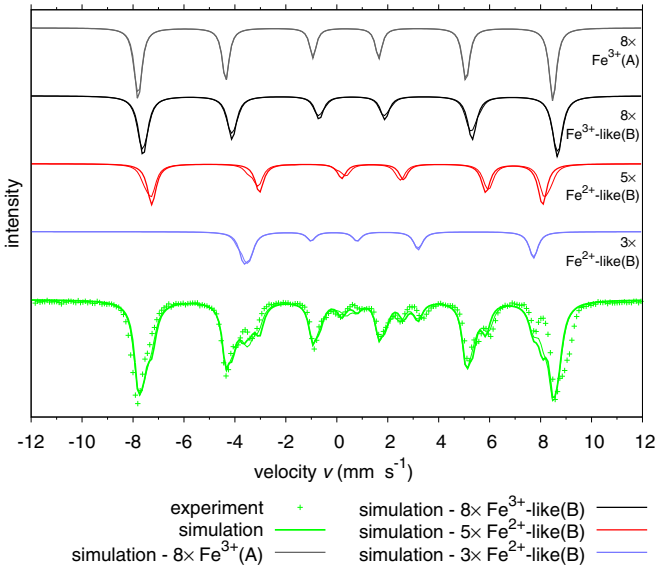

FIG. 5. Comparison of the four-sextet approximation (thick lines) with the subspectra calculated by considering individual sites in the groups (thin lines); see text for details. Black, red, and blue indicate the three groups of Fe(B) subspectra corresponding to the three groups of Fe(B) ions identified in Ref. [2]. The experimental data (see Sec. IV) are given for comparison. The spectra are referenced to α-Fe.

charge fluctuation can be expected. The result of the simulation shown in Fig. 4 can be compared to the experimental spectra of the single-domain crystal, as well as of a powder sample or a sample presented in Sec. IV because the configurations of these samples yield the same sextet line-intensity ratio [39].

The result reveals contributions of four groups of iron sites identified in Ref. [2] to the spectrum. Namely, the line near 3 mm s^{-1} described by Pasternak *et al.* [8] as a characteristic feature of the *Cc* phase spectrum can be attributed to the group of B7, B13, and B16 Fe^{2+}-like ions. The apparent difference between the subspectra of this group of ions and subspectra of other Fe^{2+}-like(B) ions illustrates the differences between the electronic configurations of these two groups of ions (see Ref. [2] for details) [40].

The spectral contributions of Fe(B) sites from the same group are very similar. This suggests a decomposition of experimental ^{57}Fe Mössbauer spectra into four sextets [8 × Fe^{3+}(A), 8 × Fe^{3+}-like(B), 5 × Fe^{2+}-like(B), and 3 × Fe^{2+}-like(B)] as a suitable approach, while indicating that identifying individual iron sites in experimental spectra is virtually impossible.

In a simple approximation, a subspectrum of each of the groups of iron ions can be replaced by a single sextet described by hyperfine parameters calculated as the average of the corresponding parameters [41] within the group (see Table IV; a detailed listing of the average EFG tensors is provided in Table V). A comparison of these four sextets with the subspectra calculated by considering individual sites in the groups is shown in Fig. 5. The correspondence is particularly good for the 8 × Fe^{3+}(A), 8 × Fe^{3+}-like(B), and 3 × Fe^{2+}-like(B) groups, while it is still acceptable for the group of five Fe^{2+}-like(B) ions, where the hyperfine parameters of the B3 and B4 sites make the subspectra of these sites slightly different from the rest of this group.

Even better agreement of the simulation with the experiment can be reached by calculating the average hyperfine magnetic fields directly from the zero-field NMR measurement at 4.2 K [12,13]; the result can be found in Fig. 6. The increased magnetic splitting of the four sextets leads to an apparent overall improvement of the match with the experimental data.

IV. EXPERIMENT

The measurement of the ^{57}Fe Mössbauer spectrum was carried out at 4 K using a thin-plate single-crystal magnetite sample. The single crystal was prepared using the skull-melting method [42] followed by subsolidus annealing in CO/CO_2 atmospheres in order to achieve the appropriate stoichiometry [43,44]. The quality of the sample was checked by the ac magnetic susceptibility measurement (the result is shown in Fig. 2 in the Supplemental Material [35]); the Verwey

TABLE IV. Average hyperfine parameters assigned to the four sextets representing the four groups of iron ions in the simulated Mössbauer spectrum (see text). See Table V for the details of the EFG tensors including principal-axis orientation.

Parameter	$8 \times Fe^{3+}$(A) (A1, A2, A3, A4, A5, A6, A7, A8)	$8 \times Fe^{3+}$-like(B) (B12, B15, B8, B5, B10, B11, B6, B9)	$5 \times Fe^{2+}$-like(B) (B4, B14, B3, B1, B2)	$3 \times Fe^{2+}$-like(B) (B7, B16, B13)
Isomer shift $\bar{\delta}$ (mm s^{-1})	0.347	0.562	0.905	0.957
Hyperfine magnetic field $\bar{B}_{hf}$ (T)	50.59	50.53	47.62	35.39
Hyperfine magnetic field based on NMR $\bar{B}_{hf}^{NMR}$ (T)	50.74	51.72	49.87	36.06
EFG $\bar{V}_{zz}$ ($\times 10^{21}$ V m^{-2})	−0.316	−0.489	−6.428	13.699
EFG $\bar{\eta}$	0.392	0.348	0.610	0.039
Line broadening (Γ_N)	1	2	2	2

transition was found at 123.1 K, indicating an almost perfect sample structure, close to the ideal stoichiometry.

The measurements of ^{57}Fe Mössbauer spectra were performed in the transmission geometry using a constant-acceleration-type spectrometer with a ^{57}Co in Rh source kept at room temperature. The spectrometer was calibrated at room temperature with a 10-μm-thick α-Fe foil. The thin plate (approximately 0.1 mm) of the magnetite crystal cut along the (001) plane (in cubic notation) was glued to the sapphire plate by wax and placed in a helium cryostat with the [001] direction (in cubic notation) parallel to the γ ray. (The Mössbauer spectrum measured above the Verwey transition temperature is presented in Fig. 3 of the Supplemental Material [35].) The sample was then cooled down to 4 K.

All possible structural domains originating from the orthorhombic and monoclinic twinnings were present in the sample since no magnetic field was used during the cooling and spectrum measurement. Taking into account the magnetization directions (close to the local c axis) in these domains with respect to the direction of the γ ray, the ratio of total line intensities of particular sextets is expected to match the one found in the simulation [45]. Note, however, that since the sample was glued to the sapphire plate, the resulting strain might affect the domain structure to some extent.

The spectrum was analyzed by means of a least-squares fitting procedure which entailed calculations of the positions and relative intensities of the absorption lines by numerical diagonalization of the full hyperfine interaction Hamiltonian [46]. The absorption line shape of the spectrum was described using a transmission integral formula [47]. The final fit was carried out in the same FITSUITE software as the simulation. The acquired spectrum is presented in Fig. 7 together with a decomposition into four components corresponding to the four groups of Fe ions. The hyperfine parameters in Table IV (using the NMR-based magnetic field values) were used as starting parameters for the decomposition fit. The fitted parameters comprised isomer shifts, hyperfine magnetic fields, EFG $\bar{V}_{zz}$ values [48], line broadenings, and total absorption, while other parameters (namely, the EFG asymmetry parameters $\bar{\eta}$ and the orientations of the EFG principal axes, as well as the γ-ray direction and relative spectral contributions of the four sextets) remained intentionally fixed. The resulting output parameters of the fit are provided in Table VI. [The EFG $\bar{V}_{zz}$ values corresponding to the groups of $8 \times Fe^{3+}$(A) and $8 \times Fe^{3+}$-like(B) ions were kept fixed because their variation within reasonable limits had a negligible impact.] Clearly, the fit reproduces all significant features of the experimental spectrum well. The small deviations from experimental peak intensities can be attributed to the influence of the strain (caused by gluing the sample) on the abundance of particular structural domain types.

Compared to the initial values, the fit yielded systematically larger isomer shifts (by up to 11%; the estimated error of isomer shift values obtained by the DFT calculations is ±4%)

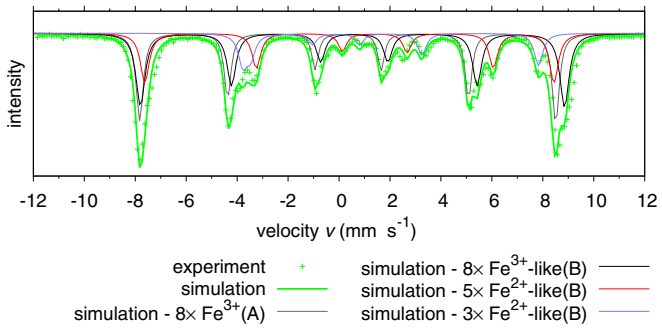

FIG. 6. The four-sextet approximation improved by taking the average hyperfine magnetic fields directly from the zero-field NMR measurement at 4.2 K [12]; see text for details. Black, red, and blue indicate the three groups of Fe(B) subspectra corresponding to the three groups of Fe(B) ions identified in Ref. [2]. The experimental data (see Sec. IV) are given for comparison. The spectra are referenced to α-Fe.

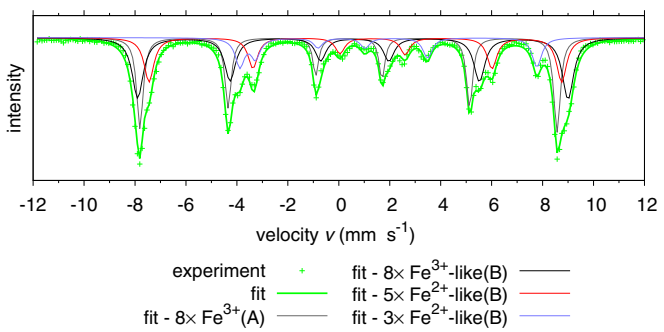

FIG. 7. Experimental Mössbauer spectrum (referenced to α-Fe) of magnetite at 4 K decomposed into four sextets by the fit (see text). The gray line denotes the sextet corresponding to the group of Fe(A) ions, while the black, red, and blue lines indicate the three sextets representing the three groups of Fe(B) ions identified in Ref. [2].

TABLE V. Average EFG tensors assigned to the sextets representing particular groups of iron ions in simulated Mössbauer spectrum. See the text for symbol definitions.

Group	$\bar{V}_{aa}$ ($\times 10^{21}$ V m^{-2})	$\bar{V}_{bb}$ ($\times 10^{21}$ V m^{-2})	$\bar{V}_{cc}$ ($\times 10^{21}$ V m^{-2})	$\bar{V}_{ab}$ ($\times 10^{21}$ V m^{-2})	$\bar{V}_{ac}$ ($\times 10^{21}$ V m^{-2})	$\bar{V}_{bc}$ ($\times 10^{21}$ V m^{-2})	$\bar{V}_{zz}$ ($\times 10^{21}$ V m^{-2})	$\bar{V}_{yy}$ ($\times 10^{21}$ V m^{-2})	$\bar{V}_{xx}$ ($\times 10^{21}$ V m^{-2})	$\bar{\eta}$	Principal axis $\vec{v}_{zz}$	Principal axis $\vec{v}_{yy}$	Principal axis $\vec{v}_{xx}$
$8 \times Fe^{3+}$(A)	−0.134	0.220	−0.086	0.000	0.205	0.000	−0.316	0.220	0.096	0.392	(0.747, 0, −0.665)	(0, −1, 0)	(-0.665, 0, −0.747)
$8 \times Fe^{3+}$-like(B)	0.299	0.160	−0.458	0.000	0.156	0.000	−0.489	0.330	0.160	0.348	(0.195, 0, −0.981)	(0.981, 0, 0.195)	(0, −1, 0)
$5 \times Fe^{2+}$-like(B)	1.244	5.174	−6.417	0.000	0.287	0.000	−6.428	5.174	1.255	0.610	(0.037, 0, −0.999)	(0, −1, 0)	(0.999, 0, 0.037)
$3 \times Fe^{2+}$-like(B)	−7.114	−6.584	13.698	0.000	0.119	0.000	13.699	−7.114	−6.584	0.039	(-0.006, 0, −1)	(1, 0, −0.006)	(0, −1, 0)

TABLE VI. Average hyperfine parameters assigned to the sextets representing the four groups of iron ions after a refinement by the fit of the experimental Mössbauer spectrum (see text). Free parameters of the fit are in bold, and the percentage in parentheses denotes the relative difference compared to the starting values in Table IV (hyperfine magnetic fields are related to the NMR-based values); all other parameters (except total absorption) were kept fixed. See Table V for the details of the orientation of principal axes of the EFG tensors.

Parameter	$8 \times Fe^{3+}$(A) (A1,A2,A3,A4, A5,A6,A7,A8)	$8 \times Fe^{3+}$-like(B) (B12,B15,B8,B5, B10,B11,B6,B9)	$5 \times Fe^{2+}$-like(B) (B4,B14,B3, B1,B2)	$3 \times Fe^{2+}$-like(B) (B7,B16,B13)
Isomer shift $\bar{\delta}$ (mm s^{-1})	**0.386** (+11%)	**0.577** (+3%)	**0.985** (+9%)	**1.018** (+6%)
Hyperfine magnetic field $\bar{B}_{hf}$ (T)	**50.88** (+0.3%)	**52.58** (+1.6%)	**50.32** (+0.9%)	**36.23** (+0.5%)
EFG $\bar{V}_{zz}$($\times 10^{21}$ V m^{-2})	−0.316	−0.489	**−4.34** (−33%)	**11.90** (−13%)
EFG $\bar{\eta}$	0.392	0.348	0.610	0.039
Line broadening (Γ_N)	**0.88** (−12%)	**3.31** (+65%)	**2.48** (+24%)	**2.13** (+7%)

and hyperfine magnetic fields (by up to 1.6%). On the other hand, the fitted EFG $\bar{V}_{zz}$ parameters are lower in absolute values than the starting ones. The significant difference of −33% in the case of the group of $5 \times Fe^{2+}$-like(B) ions can be caused by a wide range of hyperfine fields at iron sites in this group, which slightly complicates the approximation of the group subspectrum by the single sextet. Resulting line broadening values are relatively close to the initial estimation used for the simulations in the case of the groups of $8 \times Fe^{3+}$(A) and $3 \times Fe^{2+}$-like(B) ions, whereas they reach higher values for the groups of $8 \times Fe^{3+}$-like(B) and $5 \times Fe^{2+}$-like(B) ions, most likely due to the broader ranges of hyperfine fields at particular ions in these groups. The fitted total absorption is smaller than the value used for the simulation by just 3% of the value.

V. CONCLUSIONS

We have carried out DFT calculations of isomer shifts and EFG tensors for all 24 crystallographic iron sites in the low-temperature structure of magnetite. The results support the concept of trimerons [15]. The calculated data together with corresponding hyperfine magnetic fields derived from our previous work [2] form a complete set of hyperfine parameters, allowing for a simulation and deeper analysis of the Mössbauer spectrum of this compound. We have simulated Mössbauer sextets for each of the 24 iron positions and, comparing these results with the experimental spectrum, have found that the experimental line positions and all spectral subtleties are reproduced. Thus, every feature visible in the experimental Mössbauer spectrum is understood and can be explained by the *ab initio* calculated electronic structure.

Based on the 24 sextets, we have also verified our previous finding [2] that the 24 iron sites naturally break into four groups: $8 \times Fe^{3+}$(A), $8 \times Fe^{3+}$-like(B), $5 \times Fe^{2+}$-like(B), and $3 \times Fe^{2+}$-like(B) ions. The hyperfine parameters of the ions within each group share common characteristics, which means that any effort to identify individual iron sites in Mössbauer spectra is futile. On the other hand, it also allows us to approximate the spectrum by four sextets, as we demonstrated. The parameters of these four sextets, which we derived from the hyperfine parameter sets of the 24 iron positions, were further improved by determining the corresponding hyperfine magnetic fields from zero-field NMR experiments [12,13]. We thus propose those parameters as starting values for a fit of the experimental Mössbauer spectrum of magnetite.

Trying to check how good our suggestion is, we performed a Mössbauer spectroscopy measurement of a high-quality single-crystalline synthetic sample of stoichiometric magnetite. When fitting the acquired spectrum, we paid special attention to keeping the number of free parameters low to demonstrate the suitability of the four-sextet approximation. The fit matched the experimental spectrum very well, and the final hyperfine parameters are not far from the initial ones. The only limitations concerning the usability of the fit results are the probable impact of the relatively broad range of hyperfine fields at particular ion sites in the $5 \times Fe^{2+}$-like(B) group on the EFG $\bar{V}_{zz}$ value corresponding to this group and also the low sensitivity of the fit to the rather small EFG $\bar{V}_{zz}$ values of the $8 \times Fe^{3+}$(A) and $8 \times Fe^{3+}$-like(B) groups, which was the reason for keeping them fixed.

We believe that our results will serve not only for a deeper understanding of the fundamental problem of the electronic structure of magnetite but also as a tool for experimentalists who usually work from a different side of the problem trying to fit the experimental data to get parameters that give the best possible description of the processes the sample undergoes. Indeed, there are numerous situations where Mössbauer spectroscopy was used not only to solve basic problems of magnetite but also just to check for the existence of this mineral, as in many geological studies, or to suggest how geological conditions changed magnetite structure.

ACKNOWLEDGMENTS

This work was supported by the Faculty of Physics and Applied Computer Science of the AGH University of Science and Technology in Krakow. Computational resources were provided by the CESNET LM2015042 and the CERIT Scientific Cloud LM2015085, provided under the program "Projects of Large Research, Development, and Innovations Infrastructures."

[1] E. J. W. Verwey, Nature (London) **144**, 327 (1939).

[2] R. Řezníček, V. Chlan, H. Štěpánková, and P. Novák, Phys. Rev. B **91**, 125134 (2015); R. Řezníček, Ph.D. thesis, Charles University in Prague, 2015.

[3] V. A. M. Brabers, in *Handbook of Magnetic Materials*, edited by K. H. J. Buschow (Elsevier, Amsterdam, 1995), p. 189.

[4] J. M. Honig, J. Alloys Compd. **229**, 24 (1995).

[5] F. Walz, J. Phys. Condens. Matter **14**, R285 (2002).

[6] J. García and G. Subías, J. Phys. Condens. Matter **16**, R145 (2004).

[7] J. Żukrowski, A. Wiecheć, R. Zach, W. Tabiś, Z. Tarnawski, N.-T. H. Kim-Ngan, Z. Kąkol, and A. Kozłowski, J. Alloys Compd. **442**, 219 (2007).

[8] M. P. Pasternak, W. M. Xu, G. Kh. Rozenberg, R. D. Taylor, and R. Jeanloz, J. Magn. Magn. Mater. **265**, L107 (2003).

[9] B. J. Evans and S. S. Hafner, J. Appl. Phys. **40**, 1411 (1969).

[10] R. S. Hargrove and W. Kündig, Solid State Commun. **8**, 303 (1970).

[11] F. J. Berry, S. Skinner, and M. F. Thomas, J. Phys. Condens. Matter **10**, 215 (1998).

[12] P. Novák, H. Štěpánková, J. Englich, J. Kohout, and V. A. M. Brabers, Phys. Rev. B **61**, 1256 (2000).

[13] P. Novák, H. Štěpánková, J. Englich, J. Kohout, and V. A. M. Brabers, in *Ferrites: Proceedings of the Eighth International Conference on Ferrites (ICF 8)*, edited by M. Abe and Y. Yamazaki (The Japan Society of Powder and Powder Metallurgy, Kyoto and Tokyo, Japan, 2000), p. 131.

[14] M. Mizoguchi, J. Phys. Soc. Jpn. **70**, 2333 (2001).

[15] M. S. Senn, J. P. Wright, and J. P. Attfield, Nature (London) **481**, 173 (2012).

[16] M. S. Senn, I. Loa, J. P. Wright, and J. P. Attfield, Phys. Rev. B **85**, 125119 (2012).

[17] C. H. Patterson, Phys. Rev. B **90**, 075134 (2014).

[18] G. A. Sawatzky, J. M. D. Coey, and A. H. Morrish, J. Appl. Phys. **40**, 1402 (1969).

[19] C. M. Srivastava, S. N. Shringi, and M. V. Babu, Phys. Status Solidi A **65**, 731 (1981).

[20] M. Rubinstein and D. W. Forester, Solid State Commun. **9**, 1675 (1971).

[21] I. Dézsi, Cs. Fetzer, Á. Gombkötő, I. Szűcs, J. Gubicza, and T. Ungár, J. Appl. Phys. **103**, 104312 (2008).

[22] P. Blaha, K. Schwarz, G. Madsen, D. Kvasnicka, and J. Luitz, WIEN2k, *An Augmented Plane Wave + Local Orbitals Program for Calculating Crystal Properties* (Karlheinz Schwarz, Techn. Universität Wien, Austria, 2001).

[23] G. K. Wertheim, H. J. Guggenheim, and D. N. E. Buchanan, Phys. Rev. **169**, 465 (1968).

[24] M. Filatov, Coordin. Chem. Rev. **253**, 594 (2009).

[25] U. D. Wdowik and K. Ruebenbauer, Phys. Rev. B **76**, 155118 (2007).

[26] S. Sinnecker, L. D. Slep, E. Bill, and F. Neese, Inorg. Chem. **44**, 2245 (2005).

[27] E. V. Mielczarek and W. P. Winfree, Phys. Rev. B **11**, 1026 (1975).

[28] E. V. Mielczarek and D. A. Papaconstantopoulos, Phys. Rev. B **17**, 4223 (1978).

[29] O. C. Kistner and A. W. Sunyar, Phys. Rev. Lett. **4**, 412 (1960).

[30] L. R. Walker, G. K. Wertheim, and V. Jaccarino, Phys. Rev. Lett. **6**, 98 (1961).

[31] G. K. Wertheim and D. N. E. Buchanan, Phys. Rev. **161**, 478 (1967).

[32] K. J. Duff, Phys. Rev. B **9**, 66 (1974).

[33] Y. Zhang, J. Mao, and E. Oldfield, J. Am. Chem. Soc. **124**, 7829 (2002).

[34] The use of orthorhombic coordinates is convenient here since the symmetry lowering during cooling through T_V is dominated by orthorhombic deformation of the magnetite unit cell, whereas simultaneous monoclinic deformation is rather small; see Ref. [2] for details.

[35] See Supplemental Material at http://link.aps.org/supplemental/10.1103/PhysRevB.96.195124 for additional figures.

[36] The $B_{\mathrm{ani}}^{\mathrm{calc}}$ values of all A sites are lower than 2% of their $B_{\mathrm{iso}}^{\mathrm{calc}}$. Thus, the significant reduction of the corresponding anisotropy tensors by the renormalization does not impact the simulated spectrum dramatically. The difference in c_{ani} for the A and B sites is related to generally different characters of electronic and structural configurations of the A and B sites.

[37] R. F. W. Bader, *Atoms in Molecules: A Quantum Theory* (Oxford University Press, Oxford, 1990).

[38] Sz. Sajti, L. Deák, and L. Bottyán, arXiv:0907.2805.

[39] J. M. Cadogan and D. H. Ryan, in *Handbook of Applied Solid State Spectroscopy*, edited by D. R. Vij (Springer, New York, 2006).

[40] The specific shape of the $\underline{B}7$, $\underline{B}13$, and $\underline{B}16$ subspectra is a result of a merging of the sextet lines near -3.5 mm s^{-1} caused by a special orientation of the principal axes of the EFG and hyperfine field anisotropy tensors along the crystallographic axes. The reason is that minority-spin electrons occupy the xy orbitals of these sites and the axes of the trimerons in which these sites participate are parallel to the a or b axes; see Ref. [2].

[41] In the case of the EFG tensors, individual tensor elements $V_{\alpha\alpha'}$ ($\alpha,\alpha' = a,b,c$) are averaged. The ac-glide-generated sites are also taken into account, yielding average $\bar{V}_{ab}$ and $\bar{V}_{bc}$ values equal to zero.

[42] H. R. Harrison and R. Aragón, Mater. Res. Bull. **13**, 1097 (1978).

[43] R. Aragón, H. R. Harrison, R. H. McCallister, and C. J. Sandberg, J. Cryst. Growth. **61**, 221 (1983).

[44] H. Flood and D. G. Hill, Z. Elektrochem., Ber. Bunsen-Ges. Phys. Chem. **61**, 18 (1957.

[45] This can be simply illustrated by considering only the orthorhombic twinning: the domains with the c axis parallel to the γ-ray direction yield relative sextet line intensities 3:0:1:1:0:3, while the other two types of domains have the c axis perpendicular to the γ-ray direction, so they provide a sextet line-intensity ratio of 3:4:1:1:4:3. These three types of domains are present in the sample with the same probability, so together they give rise to sextets with a total relative line-intensity ratio of 3:2:1:1:2:3.

[46] N. N. Greenwood and T. C. Gibb, *Mössbauer Spectroscopy* (Chapman and Hall, London, 1971); P. Gütlich, R. Link, and A. Trautwein, *Mössbauer Spectroscopy and Transition Metal Chemistry* (Springer, Berlin, 1978).

[47] S. Margulies and J. R. Ehrman, Nucl. Instrum. Methods **12**, 131 (1961); G. K. Shenoy, J. M. Friedt, H. Maletta, and S. L. Ruby, in *Mössbauer Effect Methodology*, edited by I. J. Gruverman, C. W. Seidel, and D. K. Dieterly (Plenum, New York, 1974), Vol. 10, p. 277.

[48] In other words, all elements of a particular EFG tensor were scaled by the same fitted factor.